Coatable Splice Process in Film Coating: A Fluid Mechanical Stability Problem

Mark A. Hackler and Noel C. Brandon
DuPont Photropolymer and Electronic Materials, Parlin, NJ 08859

Robert I. Hirshburg
Sterling Diagnostics, Brevard, NC 28712

Kostas N. Christodoulou
DuPont Central R&D, Wilmington, DE 19880

In slide coating of photographic films, liquid layers flow down an inclined plane, across a small gap under a pressure differential (vacuum), and onto a fast-moving substrate. Process interruptions to allow splices of adjoining rolls of substrate to pass through the coater result in significant waste. Coating over splices fails due to air entrainment and/or two free-surface flow instabilities during the necessary gap widening: (1) standing waves (ribbing) or rupture of the liquid bridge when vacuum is kept high or (2) lateral contraction when vacuum is lowered. The problem of coating over splices is solved here by reducing it to a fluid-mechanical stability problem. First, air entrainment was eliminated by serrating the splice trailing edge and lateral contraction by prewetting the substrate with liquid streams. Avoiding rupture of the liquid bridge then reduces the problem to finding the vacuum at which the bridge becomes unstable to small disturbances. This "critical" vacuum is found by finite-element stability analysis of the quasi-steady 2-D free-surface flow to small 2-D and 3-D disturbances, direct tracking of critical points, and verification by solving the transient 2-D skip-out process. Three modes of failure are predicted if the vacuum is not sufficiently reduced with gap widening. Implementation of a computed vacuum strategy in a production line gave sufficient latitude for coating over imprecise splices.

Introduction

Slide coating is widely used in the photographic industry due to its ability to coat multiple layers of gelatin–water solutions simultaneously with good uniformity at high speeds (~ 2–3 m/s). This article reports an application of advanced fluid-mechanical stability analysis and numerical mathematics to solve an important problem in this practical, high-impact industrial process. The key steps of the slide coating process are represented in Figure 1. Coating solutions issue through narrow slots and flow down an inclined plane (slide) in laminar flow. At the end of the slide the layer stack, usually less than 1 mm in thickness, forms a liquid bridge ("coating bead") that flows across a narrow gap (Gap 2) and onto the moving substrate ("web") provided by an unwinding roll. The lower liquid/air interface of the liquid bridge separates from the slide surface at a wetting line, called the "static contact line"(SCL), and meets the fast-moving web surface at another wetting line, called the "dynamic contact line"(DCL), where it completely displaces the air entrained by the web. Although the layers on the slide are miscible, the contact time between them prior to solidification is so short that for many important species no appreciable interdiffusion takes place, allowing the layers to effectively maintain their integrity. A small pressure differential (0–250 Pa vacuum) is usually applied across the coating bead to stabilize its operation at high speeds. The coating bead is steady and transversely uniform (2-D) only in a certain range of the applied vacuum; this range of stable operation depends on all flow parameters,

Correspondence concerning this article should be addressed to K. N. Christodoulou who is currently at the Avery Demison Research Center, Pasadena, CA 91107.

but mainly on gapwidth (Christodoulou and Scriven, 1988; Christodoulou, 1990).

By operating in the desired range of coating process parameters, consistent coating quality can be maintained as long as continuous web is transported through the coating zone. However, when the current roll of web material ends, it must be spliced to a new roll without shutting down the line, which would be a costly process interruption. Usually the gap is momentarily widened by retracting the slide die or the backup roll to allow the splice to pass through the slide-to-web and the vacuum box-to-web gaps (Gaps 2 and 1 in Figure 1). This gap widening (the "skip-out") ruptures the coating bead until the normal operating gap is reestablished after splice passage. Coating materials are wasted in the interim. Moreover, the rupturing and re-forming of the coating bead causes unacceptable thickness variations, which though transitory, often persist long after splice passage causing thick patches that do not dry in an optimized dryer causing undesirable deposits on coating side rollers as well as subsequently hampering unwinding and finishing operations. As much as 3% of total coating materials can be wasted during splice passage. Therefore, coating uninterruptedly over splices offers significant savings both in material costs and in improving product quality by reducing process upsets. Other benefits of coatable splices include reduced downtime for cleaning transport rolls, fewer base creases due to dirty rolls, and fewer web tears due to tacky substrates.

Precision vs. "flying" splices

There are two types of splices: precision or "butt" splices and "flying" splices. Precision splices are made by placing the expiring roll of web end-to-end with the new web without overlapping. Coating over them is relatively easy provided the two ends have been precisely cut, positioned, and joined (usually with thin backside tape). This can only be achieved by using expensive web accumulators to bring the two ends temporarily to a halt during splicing without interrupting the coating operation.

Flying splices are made while the web is running at line speed. They are much cheaper to implement than precision splices because no web accumulator is required. A strip of two-sided adhesive tape is first applied across the outside lap of a new roll. The new roll starts rotating until its surface speed matches that of the expiring roll. The two rolls are then bumped together ("spliced") at the tape and nearly simultaneously the expiring roll is cut so that its new trailing end picks up the beginning of the new roll and carries it through the line. The thick, uneven lap splice created by this process could jam in the tight clearance of the operating gaps of the slide coater; consequently, the coating roll is typically retracted an inch or more during skip-out to accommodate the splice. When the standard gap width is restored during skip-in, the liquid bridge reforms via a transient that results in a heavy deposit at the restart of the coating. Often operator intervention is required to clean drips arising during the transient or to assist the reattachment of the coating to the edge guides (metallic strips or wire pieces that partially or completely bridge the gap, providing a surface for the liquid edges to hold on, thus enhancing their stability). On occasion, an irregularity in the static wetting line forms on the slide lip that produces a streak. A considerable quantity of web material and coating solution are wasted during such a splice passage.

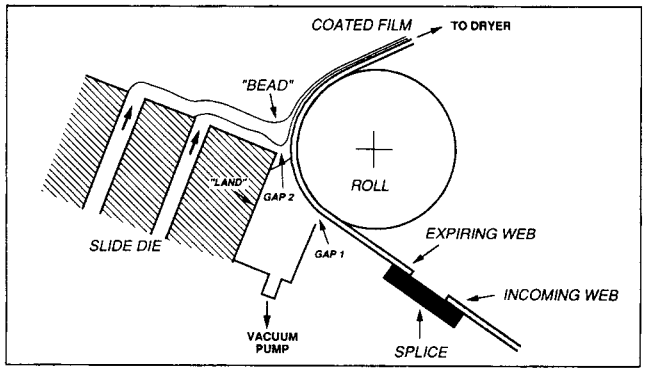

Figure 1. Prototype of a slide coater system with gap splice.

From the preceding discussion, a method of coating flying splices is greatly desired. However, a difficult problem that must be addressed for successful coating of either type of splice is *air entrainment*. Upon encountering a step-down discontinuity at the splice trailing edge, the liquid bridge undergoes continued stretching from the upper corner of the step (see Figure 1). Often, the entrained air underneath the bridge cannot escape quickly enough and as a result dynamic wetting is not reestablished and the liquid bridge ruptures. Even if a new wetting location is established, the liquid bridge can entrap air bubbles that cause flow streaks. The step-up discontinuity at the splice's leading edge generally presents less of a problem than do step-downs. In most cases, however, the splice discontinuity is sufficient to cause coating defects. Accordingly, various technologies have been developed to minimize the upset.

Special splice designs address the step-down and require precision splicing. Bourns and McDonald (1970) and Heetderks (1979) used a thick tape for mechanical strength and a thin "ramping" tape on top of it (see Figure 2a) to delay the encounter of the coating liquid with the step-down until the end of the thin tape. Kawahara et al. (1976) crimped the leading edge of the incoming roll web to allow the splicing tape to fit flush with the web surface (Figure 2b). DeRoeck and Van Steenwinkel (1980) proposed the only scheme in the patent literature that is expected to be practical with flying splice equipment: they attach the splicing tape to one side of the expiring web and to the other side of the incoming web, thus presenting the liquid bridge with only step-ups (Figure 2c). Other methods assist in displacing the entrained air by roughening the receiving substrate (Takagi et al., 1977) or by prewetting the region (Bourns and McDonald, 1970; Askew and Powell, 1968; Verkinderen et al., 1981). Fowble (1975) addresses the issue by increasing the applied vacuum immediately before and during splice passage. We will show that this strategy is only feasible for coating precision butt splices.

Clearly both flying and precision splices have serious disadvantages. In this work we propose a method that allows coating over flying splices *without* rupturing the coating bed, thus eliminating the main failing of the flying splice process. In the proposed process the die-to-web gap is momentarily increased by only a small distance (typically of the order of 1

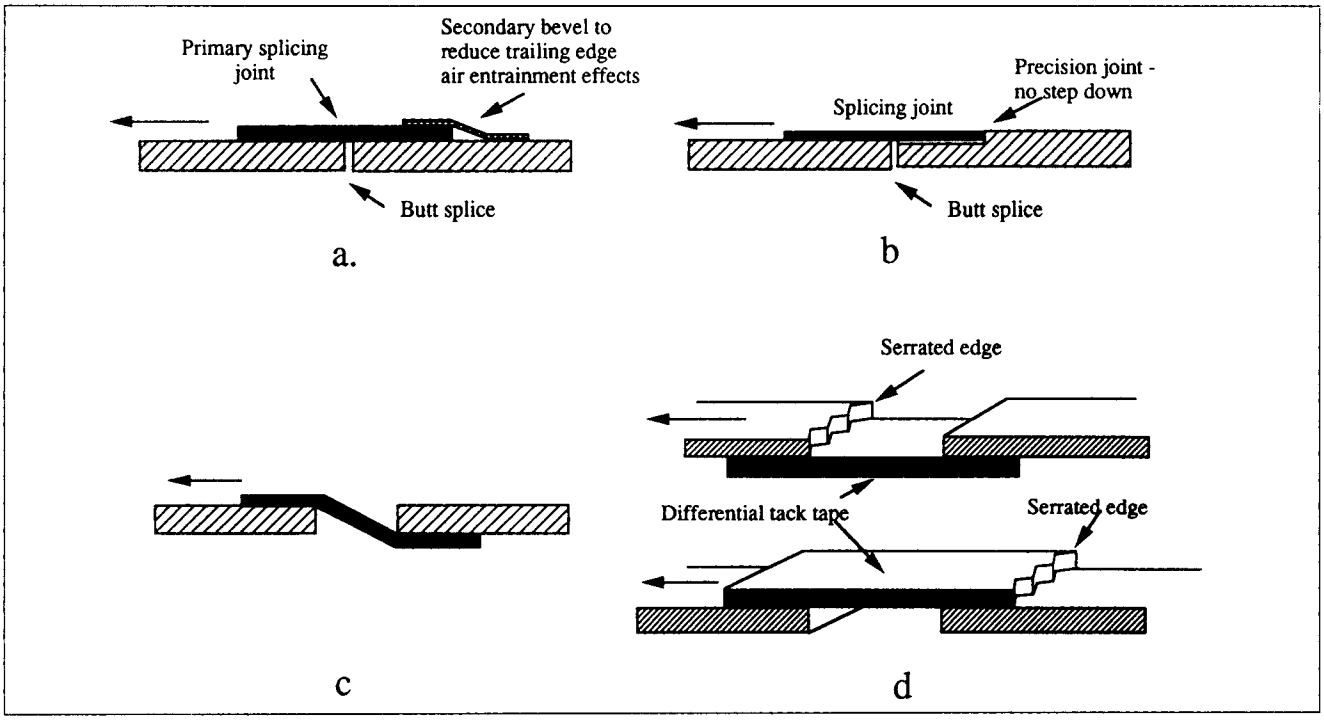

Figure 2. Splice designs.

(a) Thin "ramping" tape on top of thick tape (Bourns and McDonald, 1970; Heetderks, 1979); (b) crimped leading edge (Kawahara et al., 1976); (c) only step-ups design (DeRoeck and Van Steenwinkel, 1980); (d) serrated trailing edge (this work).

mm) that is enough to pass the splice without contact, but less than that causing coating bead rupture. This "microskip" thus avoids material waste associated with coating interruption. Four problems must be solved before such a process is successful: (1) a flying splice made at high speed must pass through the coating gap without contacting the coating slide lip; (2) air entrainment at the splice trailing edge (step-down) must be excluded or suppressed; (3) vacuum must be continuously and precisely adjusted as gapwidth is increased to avoid bead rupture; (4) the edges of the coating bead must be stabilized throughout the process.

Our flying coatable splice design and how this design solves these four problems are described in detail in the sections below. The mechanical designs for the splice and necessary slide coater modifications are presented in the following section. The air entrainment problem is addressed through this design. Even given this splice and slide coater, successful coating of splices is critically dependent on maintaining continuous coating throughout the process. Consequently the task is reduced to a fluid-mechanical stability problem of finding the critical vacuum at various gapwidths during gap opening. Both the initial indication that sufficiently wide gaps can be achieved without rupturing the coating bead and the precise vacuum reduction strategy required were provided by finite-element/linear stability analysis of the flow. This analysis is the main focus of the third and fourth sections, which include computing quasi-steady 2-D states, their stability to small 2-D and 3-D disturbances, and paths of critical points in a second parameter to define the operating window. The full nonlinear transient 2-D skip-out process is occasionally computed to verify the results of linear stability analysis. Numerical methods are briefly reviewed in the third section. In the same section a method for tracking critical points at which the ribbing instability sets in is also proposed. Computations reveal three different modes of coating failure if the applied vacuum is not sufficiently reduced during the "microskip" process (fourth section). Numerical predictions are compared with experimental data from actual splice trials in a production facility (fifth section). Conclusions and findings are summarized in the last section.

Coating Splice Process Design

Splice design configuration

A flying splice process is proposed here, in which the splicing tape bridges a wide gap between the web ends of the two rolls (see Figure 1). The key advantage of this type of splice, called a "gap splice," is that the required precisions for cut, relative positioning of the two web ends, and joining (taping) are not exacting compared with precision zero-web speed splices and can be accomplished quickly enough to be performed at line speed. The imprecision of the resultant splice, however, requires the slide-to-web gap to be momentarily increased to assure splice passage. Typically, a minimum gap of 1.3 mm is required. The liquid coating bridge becomes longer with this increased gap and thus more vulnerable to upsets. Fortunately, pressure fluctuations occurring as the splice discontinuities pass through the vacuum box lip gaps are greatly reduced since these discontinuities are now small relative to the increased clearance. Even so, under normal operating vacuum the liquid bridge ruptures at a gapwidth larger than 0.5 mm (see Figure 3). Wider gaps without bead rupture can only be achieved by lowering the vacuum as the gap is widened. Unfortunately, lowering the vacuum also causes the edges of the coating bridge to destabilize and recede, resulting in contraction of the coating width ("neck-in," "break,"

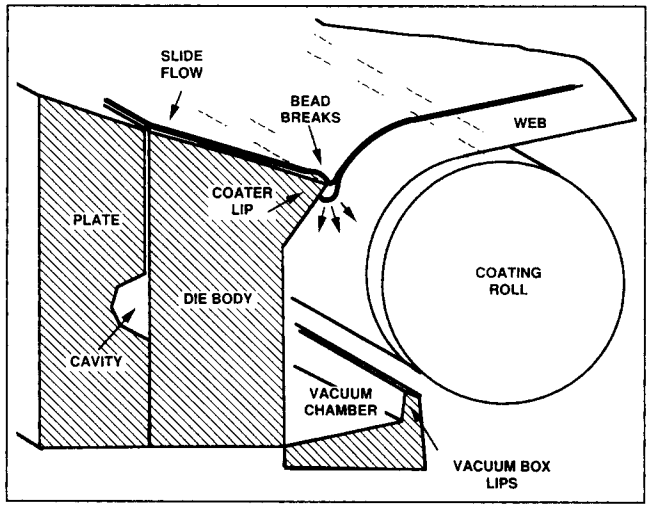

Figure 3. Liquid bridge ruptures at high vacuum.

see Figure 4). The edges of the contracted coating are heavier than before, will not dry in an optimized dryer, and thus will result in the incomplete drying-related problems mentioned previously. Our method for enhancing the stability of the coating edges at low vacuums is described next.

Coating edge stabilization

Enhancing edge stability sufficient to coat over flying splices at low vacuum pressure and wider gap requires implementation of two inventions. The first shown in Figure 5 employs small water jets impinging on the web in the slide coater vacuum chamber and positioned in-line with the liquid bridge edges (Hirshburg, 1993). The coating edges then coalesce with these precoated water lanes, resulting in a remarkable improvement in edge stability as demonstrated below. The second invention is a subtle but surprisingly effective modification to our standard edge-guide design and was proposed by one of our coating operators (W. Chodzko, personal communication). In short, the edge guides are curved toward the center of the coating, resulting in a thickening of the flow at the edge. The inertial effects of this thicker flow tend to stabilize the edge of the coating. This design, details of which are considered proprietary, was chosen among several designs, including ones that completely bridged the gap between the slide terminus and the web.

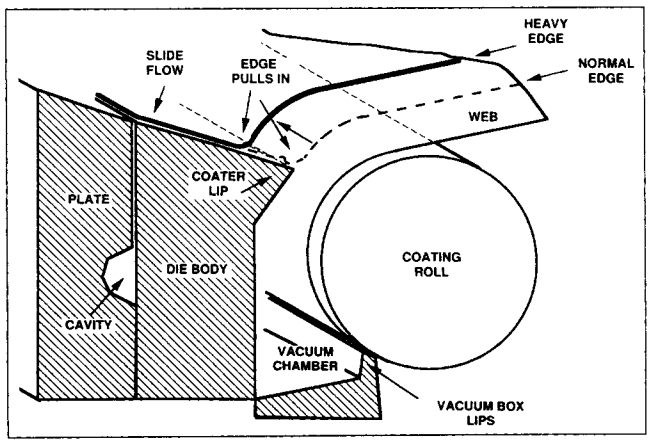

Figure 4. Edges retract at low vacuum.

Air entrainment at the trailing edge

Problems associated with air entrainment at a splice trailing edge are eliminated by serrating this edge, as shown in Figure 2d. Within practical limits, the size and pitch of the serrations are not as critical as their mere presence. Evidently, as the liquid bridge coats over the splice, it encounters step-downs only at isolated serration pits from which stretching and rewetting proceeds easily along transversely moving fronts until they coalesce again in continuous coating. Entrained air is easily excluded from the initial wetting locations and then from the edges of the expanding wetting front since air can additionally escape transversely along the serration edges. By comparison, uniform stretching and rewetting of the web simultaneously all across its width while both entrapping air in the step-down and excluding air in the direction opposite to web movement has little probability of occurring without local disturbances, and usually results in streaks or local coating rupture. With the serrated splice, good-quality coated splices are consistently achieved.

Vacuum Reduction Strategy: Finite-Element Analysis

With the edge stability and air entrainment problems solved, the final hurdle is maintaining the integrity of the liquid bridge at large gapwidths. To avoid catastrophic rupture one must carefully adjust vacuum pressure as the gap is widened. Finite-element analysis of the bead flow can supply the required vacuum-adjustment procedure from either of two model problems. The first is to investigate coating response to several different vacuum strategies during gap adjustment by solving the full nonlinear transient problem. Such trial-and-error analysis is expensive and does not readily yield the optimum vacuum strategy. The second alternative is based on the observation that the characteristic time of gap adjustment motion (order of 1 s) is much longer than the time constant of liquid bridge oscillation (~ 5 ms; see Christodoulou and Scriven, 1989). Therefore, the microskip can be treated as a quasi-static process as long as the 2-D flow remains stable with gap widening. Therefore, if the vacuum is adjusted to be successively within the operability window of steady 2-D states, the integrity of the liquid bridge will be assured. The problem is now reduced to that of finding the critical stability curve or "operability window" in the vacuum–gapwidth parameter space at which the steady uniform flow first loses stability to either 2-D or 3-D disturbances. This second route is taken below, whereas the aforementioned nonlinear transient analysis is only selectively used to verify the results of linear stability analysis.

The model of 2-D slide coating flow used here and the stability analysis to 2-D disturbances have been described in detail elsewhere (Christodoulou and Scriven, 1989). The stability to 3-D disturbances that give rise to the ribbing instability, a pattern of down-web standing waves produced, for example, when the applied vacuum exceeds an upper vacuum limit, is analyzed by Christodoulou (1990). Both of these analyses are used here to detect loss of bead stability at large gapwidths.

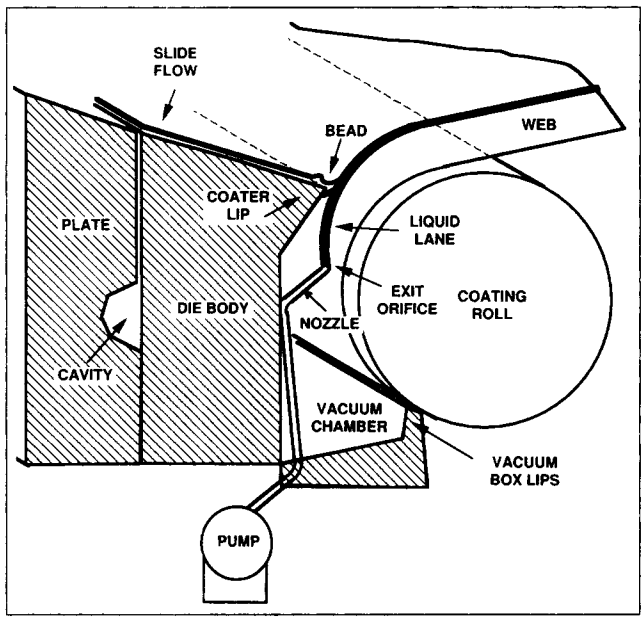

Figure 5. Lane wetters.

For completeness, the equations and boundary conditions for the general 3-D transient slide coating flow are given in Figure 6. Conservation of mass (1) and momentum (2), together with the constitutive equation for the stress in a Newtonian liquid (3) of viscosity μ, density ρ, and surface tension σ, form a Navier-Stokes system. Boundary conditions are no penetration of liquid across the free surfaces (kinematic condition (4)), capillary forces at the free surface balancing viscous fores and applied vacuum (5), and no slip at solid surfaces away from contact lines (6); (7) is Navier's slip boundary condition at and near the apparent dynamic contact line (which can be replaced by a discontinuous velocity field); (8) specifies the angle of contact of the liquid/air interface with the moving substrate surface; (9) is Gibbs' complimentarity condition at the static wetting line where the liquid/air interface meets with the stationary die wall and $\theta_D \equiv \cos^{-1}(\boldsymbol{n} \cdot \boldsymbol{n}_s)$. At the inflow boundary chosen sufficiently far upstream on the slide, (11) specifies Nusselt flow (i.e., semiparabolic velocity profile) and (12) the free-surface location. At the outflow boundary located sufficiently far downstream on the web, (13) specifies no normal traction (i.e., fully developed flow) in the streamwise direction (the effect of gravity is assumed negligible); and (14) specifies the slope of the free surface.

In the equations listed in Figure 6, $\boldsymbol{u}$ is the velocity measured in units of U, a characteristic velocity, for example, mean speed on the slide; length is measured in units of H_0, a characteristic length such as thickness of asymptotic Nusselt flow on the slide; time is measured in units of H_0/U; $\boldsymbol{i}$ and $\boldsymbol{j}$ are the unit vectors in the x and y directions; $\boldsymbol{f}$ is the unit vector in the direction of gravity; $\boldsymbol{T}$ is the stress tensor and p the pressure, both measured in units of $\mu U/H_0$; $\boldsymbol{I}$ is the unit dyadic; $Re \equiv \rho q/\mu$ is the Reynolds number, where $q = UH_0 = U_w h$ is the flow rate per unit coater width, U_w is the web speed, and h is the final film thickness; $Ca \equiv \mu U/\sigma$ is the capillary number; $St \equiv gH_0^2\rho/\mu U$ is the Stokes number, where g is the force of gravity per unit mass; $\boldsymbol{u}_s$ is the dimensionless velocity at solid boundaries; $\boldsymbol{n}$ is the local unit normal to the boundary; $H \equiv -\nabla_{II} \cdot \boldsymbol{n}/2$ is the dimensionless mean curvature of the free surface or interface, where ∇_{II} is the gradient operator on a surface (see Weatherburn, 1927); $\boldsymbol{n}_s$ is the unit normal to the solid surface; θ_s is the static contact angle; h_s is the dimensionless wetted distance from the corner to the contact line; θ_D is the dynamic contact angle; and β_{slip} is the dimensionless slip coefficient. In fact, β_{slip}, θ_D, and θ_s can be regarded as empirical parameters that must be inferred from experiments (the uncertainty in the value of β_{slip}, θ_D, and θ_s and in their variation with every other flow parameters limits the predicting capability of every coating flow model reported to date). We use constant static and dynamic contact angles and a (macroscopic) velocity field that is discontinuous at the dynamic contact line. This is accomplished by collapsing the free-surface side of the finite element adjacent to the contact line, creating a "degenerate" or "singular" element (see, e.g., Bathe, 1982, p. 226) in an attempt to capture the strong stress singularity there. Such a construction may prevent the FEM from being convergent in the pointwise sense, especially with Newtonian (i.e., nonshear-thinning) rheology. However, it was found that using a degenerate element is preferable to using a slip condition that introduces a nonphysical deceleration of the liquid as it approaches the wetting line and may pollute the macroscopic velocity field with spurious oscillations ("wiggles"). In addition, a small amount of shear thinning can make the solution convergent in the "least squares" or "energy norm." Adding such shear thinning, however, was not found to change the results appreciably.

Steady 2-D states

By means of the Galerkin finite-element method Eqs. 1–10 (Figure 6) combined with the elliptic mesh generation system of Christodoulou and Scriven (1992) are reduced into a set of M ordinary differential and algebraic equations $\boldsymbol{R}(\boldsymbol{x}, \dot{\boldsymbol{x}}, \boldsymbol{q}) = \boldsymbol{0}$ for the vector of nodal unknowns $\boldsymbol{x}$ (velocities, pressures, positions) and their time derivatives $\dot{\boldsymbol{x}}$, depending on the vector of input parameters $\boldsymbol{q}$. Steady 2-D states of this discretized set for increasing gapwidth are computed by Newton itera-

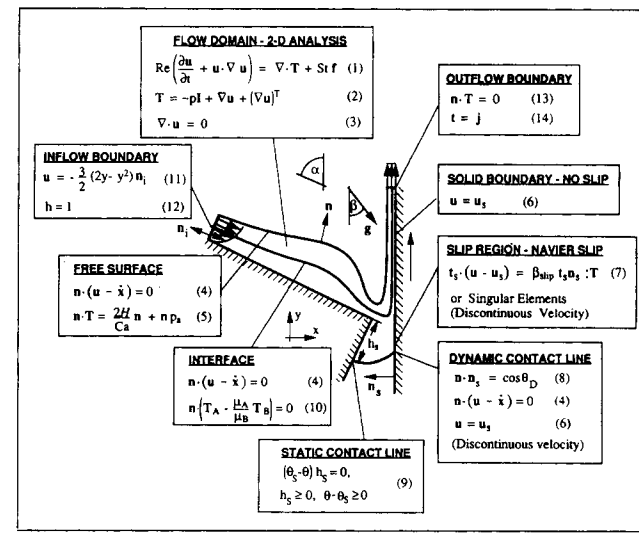

Figure 6. Governing equations and boundary conditions of slide coating flow.

tion and zero-order continuation. Where convergence of the iteration became difficult near a limit point, Abbott continuation, that is, swapping the fastest changing unknown for the continuation parameter (see Abbott, 1978), allows passing over the limit point.

Stability to 2-D disturbances

After a steady state is computed for each value of the continuation parameter q, the stability of the flow to small 2-D disturbances is assessed by assuming small disturbances of the form $\delta \boldsymbol{x} = \boldsymbol{\phi} \exp(\lambda t)$. This leads to a nonsymmetric generalized eigenvalue problem $\boldsymbol{J\phi} = \lambda \boldsymbol{M\phi}$, where $\boldsymbol{J} \equiv \partial \boldsymbol{R}(\boldsymbol{x}_0, \dot{\boldsymbol{x}} = \boldsymbol{0}, \boldsymbol{q})/\partial \boldsymbol{x}$ is the Jacobian matrix, $\boldsymbol{M} \equiv \partial \boldsymbol{R}(\boldsymbol{x}_0, \dot{\boldsymbol{x}} = \boldsymbol{0}, \boldsymbol{q})/\partial \dot{\boldsymbol{x}}$ is the mass matrix, $\boldsymbol{\phi}$ is the eigenvector, and $\lambda = \lambda_r + i\lambda_i$ the corresponding eigenvalue. Only the most dangerous part of the eigenvalue spectrum (a dozen or so eigenvalues of algebraically largest real parts) is computed by the deflated Arnoldi algorithm with "approximately exponential transformation" (see Christodoulou and Scriven, 1989). Loss of stability is detected when the leading eigenvalue (i.e., the one of largest real part) first crosses the imaginary axis, that is, λ_r turns positive. This can occur at a turning point ($\lambda_r = 0$, $\lambda_i = 0$, and $\boldsymbol{J}$ becomes singular there) or at a Hopf bifurcation point ($\lambda_r = 0$, $\lambda_r \neq 0$). If $\lambda_i = 0$ at crossing, higher-order singular points (such as bifurcation points) are possible; however, in the absence of spatial symmetries, such points exist only at unique values of a *second* input parameter (they are "nongeneric," i.e., unlikely to occur in single-parameter continuation). For parameter values beyond a turning point, no 2-D steady states exist in the vicinity of the family being followed and the liquid bridge usually breaks catastrophically. In the vicinity of Hopf points, time periodic solutions (i.e., sustained oscillations) of the flow arise.

Operability to 2-D disturbances

After a turning point has been detected, it can be computed exactly by solving the extended system of Poenisch and Schwetlick (1981) for the critical state, eigenvector, and parameter value. The same system can be used to track the turning point as a second parameter is varied. Extended systems to track Hopf points also exist but are more complicated (see Christodoulou, 1990). No Hopf points are detected in the parameter range of interest.

Stability to 3-D disturbances

A coating flow can lose stability to small 3-D disturbances before it becomes unstable to 2-D ones. A prime example is ribbing instability, which occurs as a supercritical symmetry-breaking bifurcation. While our model is defined on a 2-D mesh, it is possible to extend it to assess the stability of uniform steady flow to small 3-D (cross-web) disturbances by expanding the disturbances in Fourier modes in the cross-web direction and in the same basis functions in the xy plane as the base 2-D flow (see Ruschak, 1983; Christodoulou, 1990). The weighted residuals of the 3-D time-dependent Navier-Stokes system then reduce to another large nonsymmetric eigenvalue problem $\boldsymbol{J}_{3D}(N)\boldsymbol{\phi} = \lambda \boldsymbol{M}_{3D}(N)\boldsymbol{\phi}$, the Jacobian $\boldsymbol{J}_{3D}$ and mass matrix $\boldsymbol{M}_{3D}$ of which depend on the (dimensionless) cross-web disturbance wavenumber $N = 2\pi H_0/\Lambda$; Λ here is the disturbance wavelength. The most dangerous part of the spectrum is again computed by the deflated Arnoldi algorithm (see Christodoulou and Scriven, 1989). The wavenumber of maximum growth rate can be identified by a direct search in wavenumber. A critical parameter value to 3-D disturbances is detected when the maximum of the growth rate (λ_r) vs. wavenumber N curve first crosses zero. The corresponding wavenumber N_{cr} gives the spatial frequency of the growing waves (ribs) in the cross-web direction.

Operability to 3-D disturbances

After a critical point to 3-D instability has been detected, it is desirable to locate it exactly and to trace its path as a second parameter is varied. An extended system is proposed here whose unique solution is the point of onset of ribbing instability. This system consists of the equations for the 2-D steady flow, the eigenvalue problem for 3-D disturbances (together with a normalizing condition for the eigenvector), and the condition that the maximum growth rate at the most dangerous wavenumber vanishes:

$$\begin{gathered} \boldsymbol{R}(\boldsymbol{x}, \boldsymbol{0}, q_1) = \boldsymbol{0} \\ (\boldsymbol{J}_{3D} - \lambda \boldsymbol{M}_{3D})\boldsymbol{\phi} = \boldsymbol{0} \\ \phi_r \equiv \boldsymbol{e}_r^T \cdot \boldsymbol{\phi} = 1 \\ d\lambda/dN = 0 \\ \lambda = 0. \end{gathered} \tag{15}$$

Here $\boldsymbol{e}_r^T \equiv [0, \ldots, 0, 1, 0, \ldots 0]^T$ is the unit vector whose rth entry is unity and all others are zero. The solution of this system by a Newton-like algorithm (see the Appendix) gives the critical point: state $\boldsymbol{x}$, parameter value q_1, null vector $\boldsymbol{\phi}$, and disturbance wavenumber N.

2-D transient analysis

2-D nonlinear transient simulations are performed to validate the results of linear stability analysis. We use the differential-algebraic system solver DASSL (Petzold, 1982), which is based on a variable time-step, variable-order backward-difference method. This solver requires a linear combination of the Jacobian and mass matrices, both of which are already available from linear stability analysis. Consistent initial conditions and time derivatives needed for the index-2 differential-algebraic system (1–11 in Figure 6) are calculated by taking two first-order backward Euler steps with DASSL's time truncation error control suppressed. In the following steps variables associated with algebraic constraints, that is, pressures and coordinates of nodes other than those on free surfaces, are excluded from DASSL's time-truncation error estimation, but not from the convergence test of the Newton iteration, as suggested by Petzold and Loetstedt (1986).

Results and Discussion

The coating of interest, essentially that of a gelatin–water solution, is known experimentally to yield a stable 2-D flow. However, the wet thickness of this coating is only marginally above the minimum required for stable bead edges, as evidenced by the vulnerability of the coating flow to edge reces-

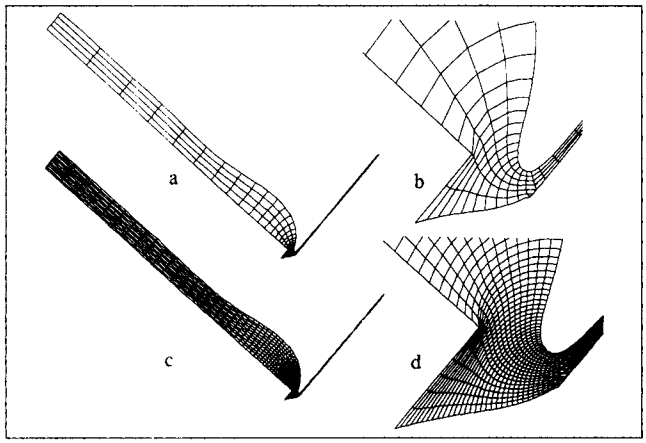

Figure 7. Coarsest and finest elliptically generated finite-element mesh in the vicinity of the coating bead.

sion. The particular coater geometry employed in this application has a lip (land) that is parallel to the surface tangent of the web at the location of coating. This has important implications in the computed operability diagram as shown below.

Starting from the base-case parameter set (see Table 1) with a gapwidth of 0.25 mm and a vacuum of 150 Pa, steady 2-D states were computed with increasing vacuum. Along the solution path, the most dangerous part of the spectrum for 2-D and 3-D disturbances was calculated. Stability to 3-D disturbances was assessed by calculating eigenvalues at various values of the cross-web disturbance wavenumber N. Starting at $N = 0$ the eigenvalue problem was solved at increasing values of N past the point at which the real part of the leading eigenvalue starts decreasing monotonically. This inevitably occurs as capillarity stabilizes modes of fine spatial structure (i.e., of large N). The first instability (ribbing) is encountered at a vacuum of 300 Pa and has a critical dimensionless wavenumber $N = 3.6$ (corresponding to a wavelength of $\Lambda = 1.6$ mm). The adequacy of the discretization was occasionally

Table 1. Parameters of Base-Case Steady State

Parameter	Units	Symbol	Base Case
Final film thickness	μm	h	40
Web speed	m/s	U_w	2.54
Pressure difference	Pa	P_b	−200
Gapwidth	mm	L	0.254
Viscosity	mPa·s	μ	18.7
Density	kg/m^3	ρ	1,100
Surface tension	mN/m	σ	35
Dynamic contact angle	deg	θ_d	130
Static contact angle	deg	θ_s	35
Slide-web angle	deg	α	90
Web-gravity angle	deg	β	−40

	Units	Base Case
Length	$h_0 \equiv [3\mu U_w h/\rho g \cos(\alpha+\beta)]^{1/3}$	0.9327 mm
Velocity	$U \equiv [\rho g U_w^2 h^2 \cos(\alpha+\beta)/3\mu]^{1/3}$	10.757 cm/s
Time	$T \equiv h_0/U$	8.671 ms

Table 2. Mesh Parameters

	M1		M2		M3		M4	
Zone	ne_x	ne_y	ne_x	ne_y	ne_x	ne_y	ne_x	ne_y
1	18	4	25	6	35	9	50	12
2	11	4	16	6	23	9	32	12
3	9	4	12	6	17	9	24	12
4	11	2	16	3	23	4	32	6

tested by successive mesh refinement, resulting in four meshes M1–M4 (Figure 7 and Table 2). Each differs by a factor of about 1.4 in each logical coordinate (i.e., by a factor of 2 in the total number of nodes) from the preceding one. Convergence with mesh refinement (see Figure 8) was found to be of first rather than third order, which would be expected of quadratic elements due to the strong stress singularity at the dynamic contact line (see also Christodoulou and Scriven, 1989).

Quasi-static model results

Figure 9 shows the computed effects of varying both gapwidth and vacuum level on bead stability. Region A represents the region where the bead is stable, and region B represents the unstable region. In general, as gapwidth is widened at fixed vacuum (or vacuum is increased at fixed gapwidth), the flow loses stability at a critical point to one of two 3-D modes, both of which lead to ribbed states. Beyond this first critical point, steady 2-D solutions of the governing system (Eqs. 1–11) exist, but are unstable to 3-D disturbances of some wavenumber range. With a further increase of gapwidth, a limit point is encountered beyond which steady 2-D states cease to exist altogether. Tracking of the critical vacuum (the so-called "upper vacuum limit") of each mode as the gapwidth is widened, gives the three curves in Figure 9. Next, each of the three modes of instability is described in more detail.

Structure of the Ribbing Modes. Consider the first ribbing mode found earlier at the base-case gapwidth of 0.25 mm and a vacuum of 300 Pa. Figure 10a shows a small free-surface perturbation in the direction of this mode, and Figure 10b

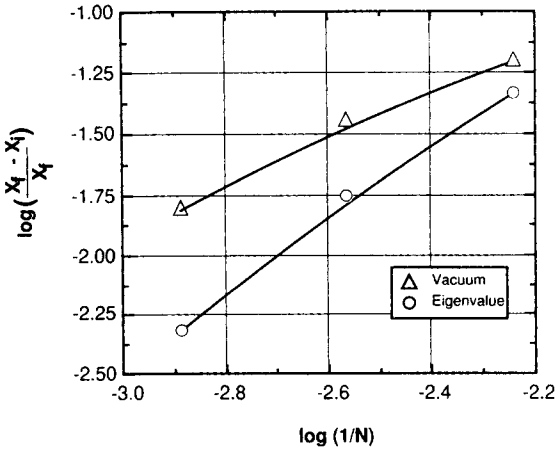

Figure 8. Convergence of computed critical vacuum with mesh refinement.

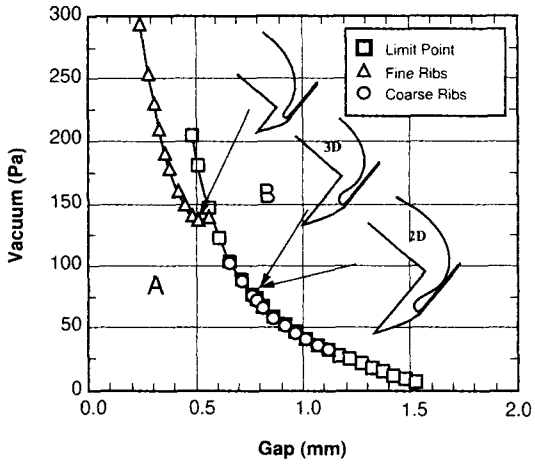

Figure 9. Process operability diagram: critical vacuum vs. gapwidth.

shows contours of its cross-web (z-) velocity component. This velocity component, which is responsible for the growth of 3-D disturbances, attains three maxima of alternating sign in the vicinity of the trough of the upper meniscus: the first two are on either side of the trough under the free surface; the third is exactly at the free surface where the film starts its exponential-like approach to its asymptotic thickness on the web.

This ribbing mode should be contrasted to the ones encountered in other flows such as in air displacing liquid from between parallel plates, the so-called Hele–Shaw flow, and forward roll coating (see Christodoulou, 1990). Those are lubrication-type flows with a significant symmetry component. Pitts and Greiller (1961) and Savage (1977a,b) give a simplified criterion for ribbing in such flows, according to which the destabilizing z-velocity component is created by a sufficiently positive (i.e., adverse) pressure gradient normal to the meniscus generated by the lubrication-type flow in the narrow gap. Christodoulou (1990) finds that in such flows the z-velocity component of the critical mode has only one maximum located at the free surface. By contrast, slide coating flow is an inherently asymmetric flow in which a higher mode —with three rather than just one extrema—is the most unstable one. Pressure contours of the steady 2-D state (Figure 10c) show that the pressure gradient under the upper meniscus is positive (adverse) only in two regions and in directions that are oblique to the free-surface normal. Large free-surface perturbations originate in the vicinity of these regions (see Figure 10a).

This first ribbing mode persists for a range of gapwidth between 0.25 and 0.56 mm, and has a critical wavenumber of $N > 3$. Its neutral stability curve is labeled "fine ribs" in Figure 9. At gapwidths above 0.66 mm, a different 3-D mode was encountered with $N = 0.4$ ($\Lambda = 14.7$ mm); its neutral stability curve is labeled "coarse ribs." Figures 11a, 11b show the free-surface perturbation and z-velocity component of this mode at a gapwidth of 1 mm, and Figure 11c shows pressure contours of the steady 2-D state. In this mode the second maximum in the z-velocity component is localized in the vicinity of the DCL, whereas the other two maxima are under the upper meniscus, as in the first mode.

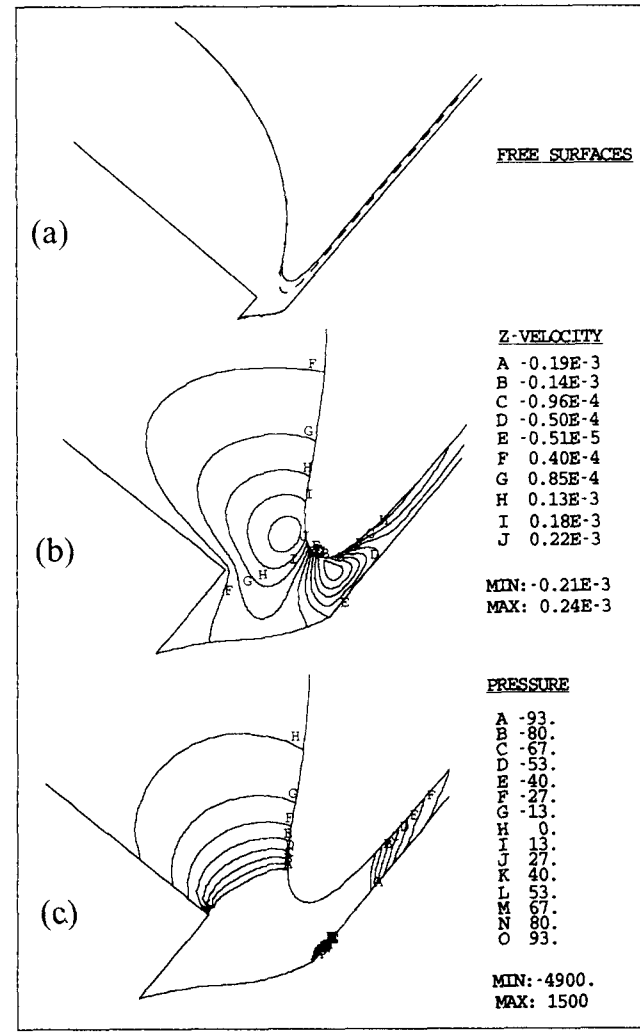

Figure 10. Most dangerous mode at gapwidth of 0.25 mm.

(a) Small free-surface perturbation in the direction of the leading mode; (b) contours of the cross-web velocity component of leading mode; (c) pressure contours of steady state.

Closer examination to establish the origin of these two distinct modes of instability is presented in Figure 12. Here, the growth rate (i.e., the real part) of the most dangerous eigenvalue is plotted against the wavenumber for two different gapwidths of 0.5 mm (square symbols) and 0.75 mm (triangle symbols). The vacuum level in each case was set to the critical vacuum for ribbing. Clearly, the growth rate vs. wavenumber curve at 0.5-mm gapwidth (square symbols) has two maxima at $N = 0.2$ and $N = 3.5$. The growth rate vs. wavenumber curve at 0.75-mm gapwidth has a first maximum at $N = 0.5$, whereas it has a shallow second maximum at $N = 4.5$. From these results and additional computations not reported here it was concluded that the two ribbing modes are actually the same 3-D mode whose growth rate has two distinct local maxima, one of which becomes critical at a different gapwidth and wavenumber. In the vicinity of the critical maxima this 3-D mode is real (filled symbols), but becomes complex (open symbols) away from them.

Limit Point. The curve labeled "limit point" (Figure 9) is established by detecting the loss of convergence of the New-

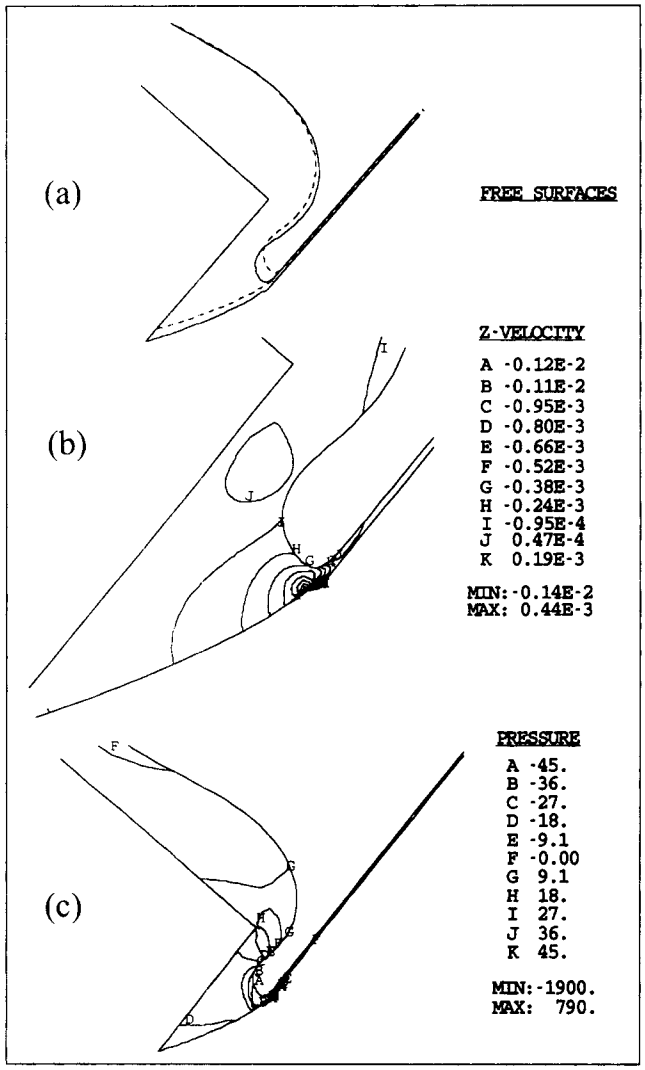

Figure 11. Most dangerous mode at gapwidth of 1 mm.

(a) Small free-surface perturbation in the direction of the leading mode; (b) contours of the cross-web velocity component of leading mode; (c) pressure contours of steady state.

ton iteration with increasing vacuum or gapwidth. In the absence of spatial symmetries such loss of convergence typically signals the existence of a turning point nearby. Surprisingly, this is not the case here. Convergence was restored by converting the DCL position into the continuation parameter via Abbott's continuation and calculating the corresponding gapwidth at a constant vacuum of 110 Pa. This procedure revealed steady states in which the DCL is drawn deep into the gap. Figure 13 shows the computed gapwidth vs. DCL position and flow profiles with small free-surface perturbations in the direction of the leading mode at representative points. The leading eigenvalue along this path of steady states approaches zero, but never changes sign. Ultimately, convergence is lost because of excessive mesh distortion. The solution surface at this point is a degenerate type of turning point, a "near" turning point, where the parametric path of steady states turns halfway (by approximately 90°) rather than turning back on itself. No uniform 2-D solutions exist beyond, and so this "nongeneric" turning point is a limit point. The

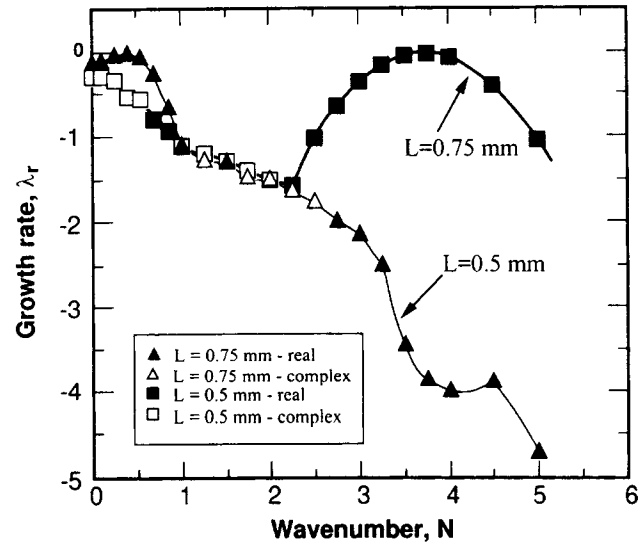

Figure 12. Dimensionless growth rate of most dangerous mode vs. dimensionless wavenumber N at gapwidth $L = 0.5$ mm and $L = 0.75$ mm showing two maxima below $N = 0.5$ and above $N = 4$.

computed flow profiles in the vicinity of this limit point shown in Figure 13 reveal that the liquid flows far down the slide lip (called "land"), across the gap and onto the moving web. As the upper free-surface meniscus is drawn deeply into the gap, its curvature remains relatively constant. Apparently the flow in the vicinity of this meniscus is nearly invariant to translation in the direction parallel to the web (although, on a larger scale, the computed upper free surface soon intersects that of the web) thus explaining the extreme sensitivity of the wetting line position and of the whole liquid bridge to the applied vacuum. Evidently, the cause of this unusual type of

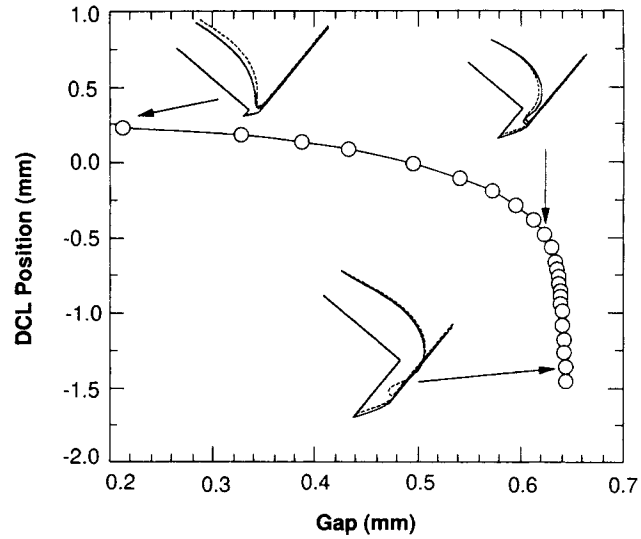

Figure 13. Computed gap as a function of DCL position with flow profiles and free surface perturbations in the direction of the most dangerous mode.

limit point is the particular lip geometry, in which the slide-die and web are idealized as parallel surfaces.

Since the leading eigenvalue does not change sign along the steady-state solution path, the usual algorithms for tracking turning points are not applicable in this case. However, one can capitalize on the insensitivity of vacuum to the DCL position in the vicinity of this limit point (see Figure 13). Indeed, a good approximation to the limit curve was obtained by fixing the DCL at 1.3 mm below the lip and calculating the corresponding vacuum for various gapwidths. To make sure that the continuation path is close enough to the curve of limit points, the leading eigenvalue was monitored; indeed, it remained close to zero (Figure 14). Had this eigenvalue drifted away from zero, it would have been necessary to fix the DCL at a deeper location in the gap.

Operability Limits. All critical curves from our model are combined in Figure 9 to define the operability limits with respect to all disturbances in the gapwidth–vacuum space. These operability limits determine the maximum vacuum ("upper vacuum limit" or UVL) at a specified gap that can be imposed on the liquid bridge before an instability sets in. There can also be a lower vacuum limit (LVL), usually characterized by edge instability and subsequent coating width contraction, but sometimes by air entrainment, barring, or ribbing. In the range of parameters of interest in this work, the LVL is marked only by edge instability, which is avoided by a combination of lane wetters and specially designed edge guides as described earlier. No other LVL is detected down to zero vacuum.

Process vacuum

According to Figure 9, to maintain stable coating while increasing gapwidth, vacuum must be reduced to remain within the envelope of stable states. However, the vacuum chamber is assembled with the slide such that as the slide-to-web gap is increased, vacuum chamber clearances also increase (e.g., Gap 2 in Figure 1), allowing increased air flow into the vacuum chamber and corresponding reduced vacuum. The simplest way to reduce vacuum during microskip then is to disable automatic vacuum control. Certainly, superior automatic control strategies could be implemented, but these would add significant complexity and cost to the process. With automatic control disabled, the question arises whether this passively controlled vacuum remains below the UVL curve throughout the microskip process.

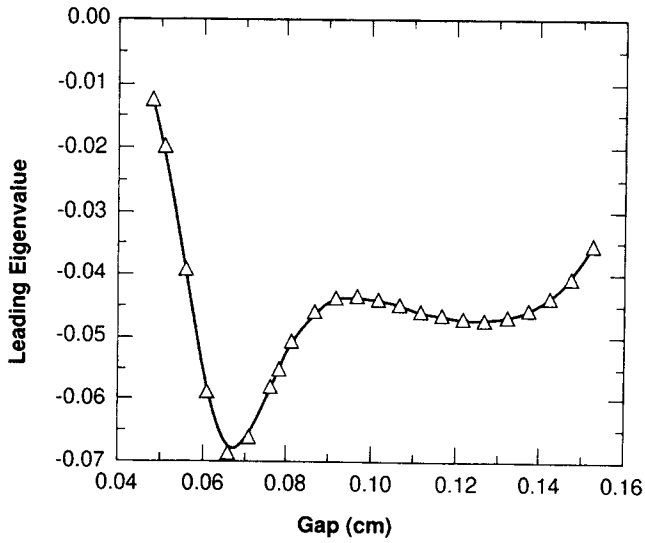

Figure 14. Leading eigenvalue along the computed curve of " near" turning points.

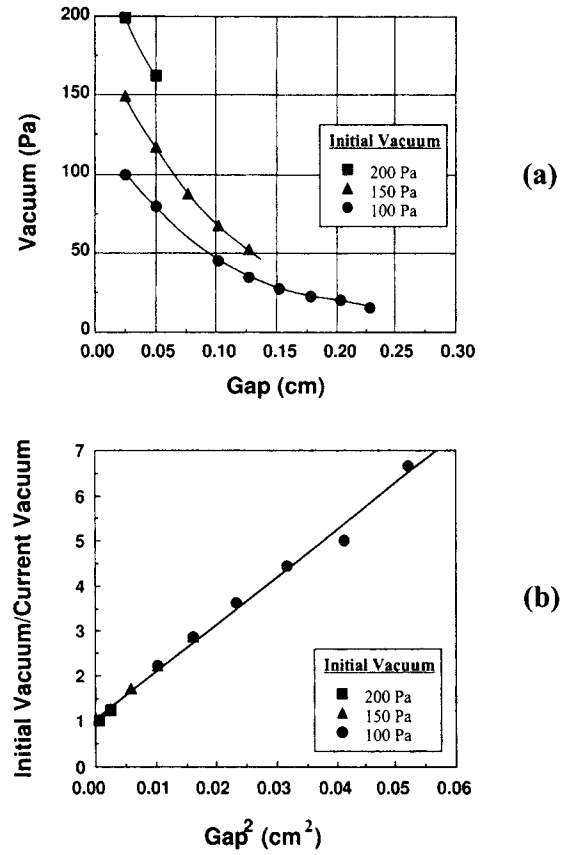

Figure 15. (a) Measured process vacuum vs. gapwidth during stable coating for three values of initial vacuum at standard gapwidth of 0.25 mm; (b) inverse vacuum vs. square of gapwidth.

Figure 15a shows the measured process vacuum vs. gapwidth during steady-state coating. For our coater geometry, the three curves correspond to different values of initial vacuum measured at a standard gapwidth of 0.25 mm. In Figure 15b, the inverse of process vacuum is plotted against the square of the gapwidth. For all three values of the initial vacuum, all points fall on a single master curve, indicating that the vacuum box gaps operate like an orifice through which the volumetric flow rate (Q) varies as the square root of applied pressure drop (ΔP). The operating limits of the microskip process are the intersections of the process vacuum curves with the UVL curves of Figure 9. The two sets of curves, combined in Figure 16, show that with an initial vacuum of 200 Pa (standard for the particular product) the maximum gap before the liquid bridge ruptures is around 0.50 mm, usually not wide enough to pass a splice (ribs already appear at 0.35 mm; there is a tacit assumption here that the ensuing 3-D state will cease to exist at or close to the limit point of 2-D states). However, with 50-Pa initial vacuum,

skip-out to 1.5 mm is possible, which is wide enough to pass splices.

Transient model concurrence

The adequacy of the quasi-static approximation and subsequent predictions of linear stability analysis to 2-D disturbances were tested by computing the 2-D nonlinear transient process of skip-out. In the two cases shown next, gap widening by 3.5 mm takes place in 1 s; this includes a linear ramp-up from rest to a maximum gap-widening speed (occurring over 1/100 of total gap change distance), a constant widening speed period, and a ramp-down to zero speed (also occurring over 1/100 of the total gap-change distance).

Figure 17 shows the liquid bridge at constant time increments during this gap-widening sequence with an initial vacuum of 200 Pa. The evolution is indeed slow (quasi static) until the gap approaches 0.5 mm; then the standing wave at the end of the slide suddenly surges and soon makes contact with the coated film on the web. At the same time the lower meniscus is drawn deeply into the gap. Therefore, gap widening to even 0.55 mm is predicted to be at best only barely feasible before air engulfment and bead rupture takes place. The same scenario, but for an initial vacuum of 50 Pa is shown in Figure 18. In this case a gap change to 1.8 mm is possible before the liquid bridge gets drawn into the vacuum box and eventually ruptures. In this case the upper meniscus never makes contact with the coated film on the web. Evidently, to achieve a gap sufficiently wide to pass the splice without bead rupture, the initial vacuum has to be dropped to 50 Pa with our coater geometry. Of course, successful gap opening does not guarantee that the liquid bridge will recover from the actual splice passage. Below, an attempt is made to verify these predictions experimentally.

Experimental Demonstration

The tests reported here were performed at DuPont's Parlin, New Jersey, production facility. First, the effectiveness of certain edge stabilization aids and their combinations is discussed, then the results are presented of a second study whereby the best combination was used in actual splice passage. As mentioned before, the low wet thickness of the coating of interest (Table 1) provided a challenging test case. In all trials automatic vacuum control was disabled during microskip, allowing vacuum to passively adjust with gapwidth. The effectiveness of various edge-stabilization aids can be assessed by either of two criteria: the lower vacuum limit below which edge recession occurs at normal operating gap, or the largest gap above which edge recession occurs at fixed vacuum. The second measure is preferred for evaluating coatable splice processes because it is desirable to make the gap as wide as possible to pass the splice without splice–coater contact. Accordingly, the gapwidth was increased gradually from 0.25 mm until the edges receded. Figure 19 shows measurements of the maximum gapwidth achieved in this way with different stabilization aids and their combinations. With standard edge guides the maximum gap was 0.64 mm, but with lane-wetters the maximum gap was 1.5 mm. In each case, the failure was edge recession. Modified edge guides alone allowed a gap of 1.3 mm, and when used in combination with lane wetters produced a remarkable 1.8–2.3-mm maximum gapwidth. Evidently, the edge-guide modification has a significant effect on the maximum gap; furthermore, this benefit is substantially additive to that of lane wetters. With edges stabilized with the combination of modified edge guides and lane wetters, microskips to large gaps without splices were achieved. In these tests, the failure at the maximum gap was not edge recession, but a global break up of the coating bead, indicating that edge stability is no longer the limiting factor.

The agreement of the theoretical predictions of Figure 16 with these microskips is quite good, especially when one ac-

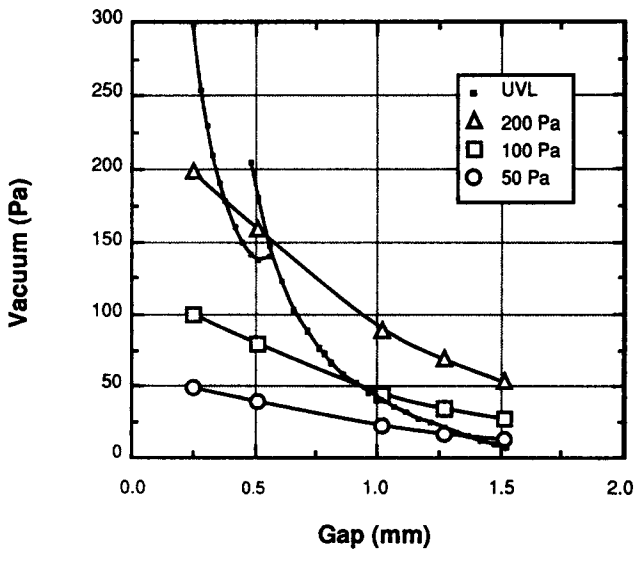

Figure 16. Combined UVL and process vacuum curves.
Intersections define maximum attainable gap before bead instability for each initial vacuum.

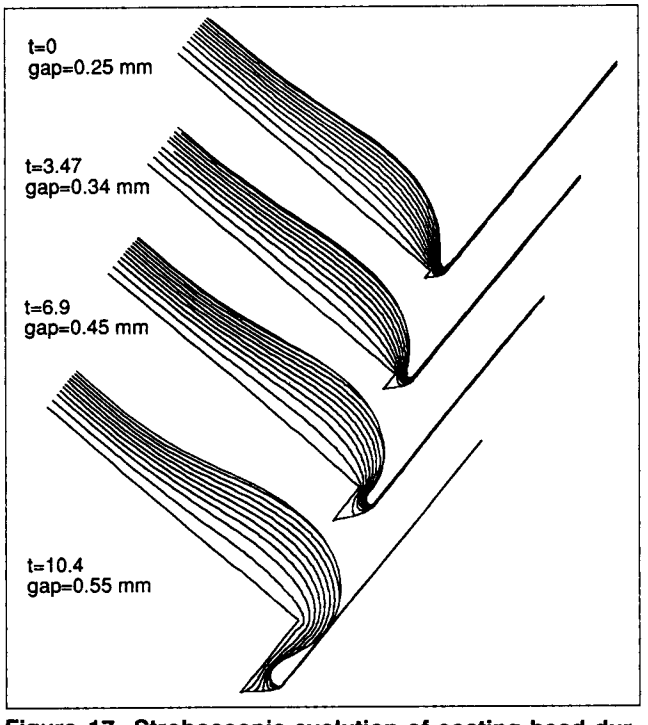

Figure 17. Stroboscopic evolution of coating bead during skip-out with an initial vacuum of 200 Pa.
Unit of time is 8.7 ms.

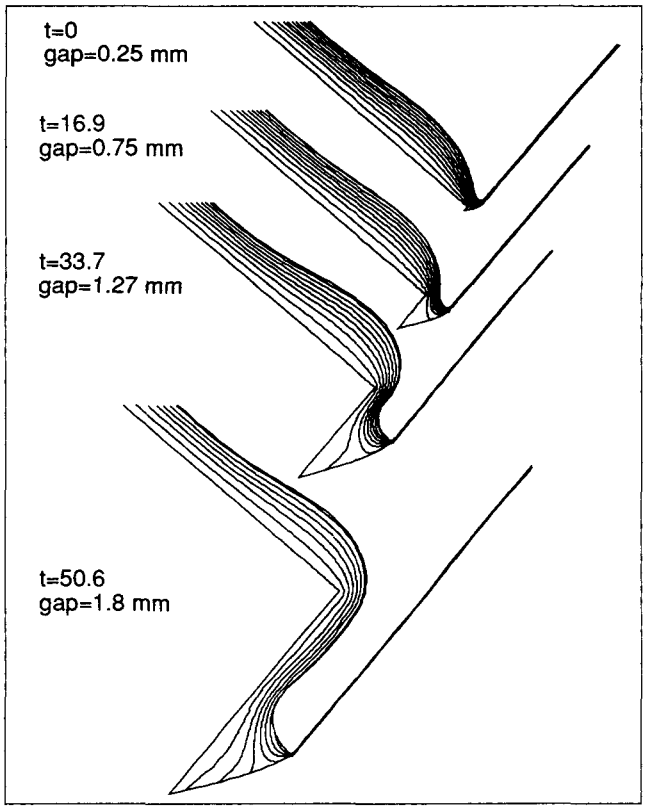

Figure 18. Stroboscopic evolution of coating bead during skip-out with an initial vacuum of 50 Pa.
Unit of time is 8.7 ms.

counts for the uncertainty in the value of the contact angles and the fact that at large gapwidths the process and UVL curves intersect almost tangentially (thus small erorrs in either curve cause large errors in the predicted maximum gap).

Splice passage

With demonstrated ability to microskip to wide gaps of 1.8–2.3 mm without bead rupture, the next step was to attempt to coat splices. Trials included at least three levels of initial vacuum shown in Figure 16 (200, 100 and 50 Pa). As predicted, the liquid bridge consistently ruptured during microskips starting at 200 Pa at gaps too small to safely attempt a splice passage. At 50 Pa, the liquid bridge ruptured at 1.3 mm, but healed once the gap and vacuum were restored. Trials at lower vacuum resulted in poorer performance. At 100 Pa, splices coated reasonably well using a microskip to 1.3 mm. The coating was disturbed slightly immediately after the "step down," but the disturbance disappeared within 3.2 mm measured from the dried coated samples.

Interestingly, it is a common practice in precision splicing to increase the applied vacuum during splice passage in order to achieve improved results (see Fowble, 1975). Indeed, by using a 2-D model similar to the one presented here (first presented by Hackler et al., 1994) to simulate actual splice passage and wetting-line advancement over smooth splices without gap change, Nagashima and Scriven (1994) show that increasing vacuum during precision-splice passage accelerates the recovery rate. By contrast, in the proposed process applied vacuum must be reduced in order to avoid catastrophic liquid bridge failure, given the necessity of a microskip for flying splice passage through the coater. However, the experiments reported here show that a small but nonzero vacuum is necessary for bead recovery after the actual splice passage. Such a prediction was not attempted by a finite-element analysis because of the as yet unresolved physics associated with the dynamic contact line.

Summary and Conclusions

A method is presented for making and coating splices in slide coating of photographic films using standard flying splice equipment. In fact, the first flying coatable splice (slide coating) process in DuPont was demonstrated on one of the most difficult to coat products. The proposed method is based on momentarily lowering the applied vacuum and widening the gap to 1.3–2.3 mm during splice passage. Finite-element/linear stability analysis of the steady 2-D flow gave the first indication of feasibility of the process as well as vacuum reduction strategies for avoiding bead rupture. Increased air leakage during gap widening can cause the vacuum to drop automatically, but this alone was shown to be insufficient control to remain below the upper vacuum limit of the liquid bridge unless the initial vacuum is lowered. Edge recession at low vacuum is avoided by using a combination of lane wetters and specially modified edge guides. Higher vacuum levels such as those used during the skip-in process, were found to rupture the bead during our momentary gap increase, in agreement with the finite-element analysis that predicts that no 2-D states exist at large gapwidth and high vacuum.

Clearly, there is an intricate coupling between splice design, surface preparation, and operating strategy, and our combination of experimental and theoretical techniques helps to understand this coupling. The new process offers many of the benefits of coatable-splice processes based on precision splices, but with significant capital savings, particularly in retrofitting existing facilities. This work is an example of how computational and experimental methods can be combined into a powerful tool for inventing and improving liquid flow processes with at least one microscopic dimension that makes either approach alone only partially successful at best. The model reported here will be extended to resolve the physics of the wetting process to predict the actual splice passage and the phenomenon of air entrainment.

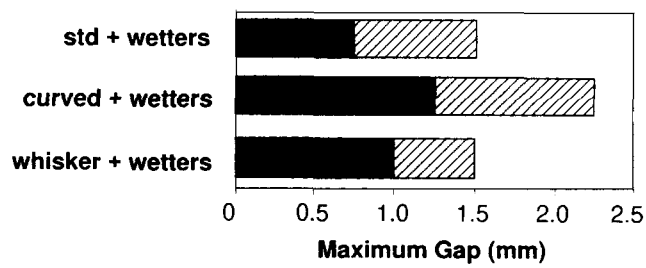

Figure 19. Measured maximum gapwidth at bead rupture with various stabilization aids and their combinations.

Literature Cited

Abbott, J. P., "An Efficient Algorithm for the Determination of Certain Bifurcation Points," *J. Comput. Appl. Math.*, **4**, 19 (1978).

Askew, W. S., and P. G. Powell, "Manufacture of Coated Layers," U.K. Patent No. 1,243,663: Kodak Limited, London (1968).

Bathe, K. J., *Finite Element Procedures in Engineering Analysis*, Prentice Hall, Englewood Cliffs, NJ (1982).

Bourns, R. T., and L. G. McDonald, "Method of Applying Photographic Coatings to a Moving Web with a Spliced Joint," U.S. Patent No. 3,518,141: Eastman Kodak, Rochester, NY (1970).

Christodoulou, K. N., "Computational Physics of Slide Coating Flow," PhD Diss., Univ. of Minnesota, Minneapolis (1990).

Christodoulou, K. N., and L. E. Scriven, "Finding Leading Modes of a Viscous Free Surface Flow: An Asymmetric Generalized Eigenproblem," *J. Sci. Comput.*, **3**, 355 (1988).

Christodoulou, K. N., and L. E. Scriven, "The Fluid Mechanics of Slide Coating," *J. Fluid Mech.*, **208**, 321 (1989).

Christodoulou, K. N., and L. E. Scriven, "Discretization of Free Surface Flows and Other Free Boundary Problems," *J. Comput. Phys.*, **99**, 39 (1992).

DeRoeck, J. I., and F. Van Steenwinkel, "Continuous Coating of Webs Having Spliced Joints," U.S. Patent No. 4,235,655: Agfa-Gevaert N.V., Mortsel, Belgium (1980).

Fowble, W. F., "Method of Coating a Spliced Web," U.S. Patent No. 3,916,043: Eastman Kodak, Rochester, NY (1975).

Hackler, M. A., N. C. Brandon, R. I. Hirshburg, and K. N. Christodoulou, "Coatable Splice Process in Photographic Film Coating: Theoretical Prediction and Experimental Investigation of Process Latitude," AIChE Meeting, Atlanta, GA (1994).

Heetderks, J. P., "Spliced Web Adapted for Coating with Liquid Coating Compositions," U.S. Patent No. 4,172,001: Eastman Kodak, Rochester, NY (1979).

Hirshburg, R. I., "Predicted Substrate for Slide Bead Coating," European Patent Application EP 57587 (12/29/1993).

Kawahara, S., A. Takagi, and H. Nozawa, "Coating Method," U.S. Patent No. 3,972,762: Fuji Film Co., Minami-ashigara, Japan (1976).

Nagashima, K., and L. E. Scriven, "Splice Passage Phenomenon in Slide Coating Flow," Coating Process Fundamentals Program, Univ. of Minnesota, Minneapolis (1994).

Petzold, L. R., "A Description of DASSL: A Differential/Algebraic System Solver," *SAND82-8637*, Sandia National Laboratories, Livermore, CA (1982).

Petzold, L. R., and P. Loetstedt, "Numerical Solution of Nonlinear Differential Equations with Algebraic Constraints II: Practical Implications," *SIAM J. Sci. Stat. Comput.*, **7**, 720 (1986).

Pitts, E., and J. Greiller, "The Flow of Liquid Films Between Rollers," *J. Fluid Mech.*, **11**, 33 (1961).

Poenisch, G. D., and H. H. Schwetlick, "Computing Turning Points of Curves Implicitly Defined by Nonlinear Equations Depending on a Parameter," *Computing*, **26**, 107 (1981).

Ruschak, K. J., "A Three-Dimensional Linear Stability Analysis for Two-Dimensional Free Boundary Flows by the Finite Element Method," *Comp. Fluids*, **11**, 391 (1983).

Savage, M. D., "Cavitation in Lubrication: 1. On Boundary Conditions and Cavity-Fluid Interfaces," *J. Fluid Mech.*, **80**, 743 (1977a).

Savage, M. D., "Cavitation in Lubrication. Part 2. Analysis of Wavy Interfaces," *J. Fluid Mech.*, **80**, 757 (1977b).

Takagi, A., S. Kawahara, and H. Takeda, "Methods for Coating Running Webs Having Projecting Splices," U.S. Patent No. 4,024,302: Fuji Film Co., Minami-ashigara, Japan (1977).

Verkinderen, P. A., L. H. Verhoeven, L. A. Christiaen, C. F. Pira, and M. L. Marckx, "Method for the Continuous Coating of Webs Having Spliced Joints," U.S. Patent No. 4,269,647: Agfa-Gevaert N.V., Mortsel, Belgium (1981).

Weatherburn, C. E., *Differential Geometry of Three Dimensions*, Cambridge Univ. Press, London (1927).

Appendix: Algorithm for Tracking Onset of Ribbing Points

A Newton-like algorithm is proposed here for the solution of the extended system (Eq. 15) that can track the onset of the ribbing instability as a parameter is varied. Straightforward solution of this system by Newton's method would require the LU-decomposition of an approximately $(3M)\times(3M)$ matrix (Eq. 15d itself is defined through an $M \times M$ system). Instead, one can take advantage of the fact that ϕ and λ do not appear in Eq. 15a, that is, equation system 15 has a block structure. The algorithm we propose here is a direct extension of one of Abbott's (1978) turning point tracking methods:

With k the iteration number,

$$\boldsymbol{y}^k \equiv \begin{bmatrix} \boldsymbol{x}^k \\ q_1^k \end{bmatrix}$$

the solution vector augmented with the parameter q_1,

$$\boldsymbol{B} \equiv \begin{bmatrix} \boldsymbol{R}_y \\ \boldsymbol{e}_r^T \end{bmatrix}$$

the augmented Jacobian matrix, where $\boldsymbol{e}_r^T \equiv [0, \ldots, 0, 1, 0, \ldots, 0]$ (the 1 is at the rth position):

1. Solve

$$\boldsymbol{B}(\boldsymbol{y}^k)\boldsymbol{s}^k = \begin{bmatrix} -\boldsymbol{R}(\boldsymbol{y}^k) \\ 0 \end{bmatrix}$$

for $\boldsymbol{s}^k$, set $\boldsymbol{z}^k = \boldsymbol{y}^k + \boldsymbol{s}^k$ (Newton update)

2. Solve $\boldsymbol{B}(\boldsymbol{z}^k)\boldsymbol{v}^k = \boldsymbol{e}_{n+1}$ for $\boldsymbol{v}^k$ (tangent vector)

3. Solve $\boldsymbol{J}_{3D}\boldsymbol{\phi} = \lambda \boldsymbol{M}_{3D}\boldsymbol{\phi}$ at $\boldsymbol{z}^k$ and wavenumbers N, $N-\epsilon$, and $N+\epsilon$, for $\lambda(N)$, $\lambda(N+\epsilon)$, $\lambda(N-\epsilon)$

4. Calculate

$$\frac{d\lambda}{dN} \simeq \frac{\lambda(N+\epsilon)-\lambda(N-\epsilon)}{2\epsilon},$$

$$\frac{d^2\lambda}{dN^2} \simeq \frac{\lambda(N+\epsilon)-2\lambda(N)+\lambda(N-\epsilon)}{\epsilon^2}$$

5. Repeat Steps (3) and (4) at $\boldsymbol{z}^k + \epsilon'\boldsymbol{v}^k$ to solve for

$$\lambda', \quad \frac{d\lambda'}{dN}, \quad \frac{d^2\lambda'}{dN^2}$$

6. Calculate

$$\frac{d\lambda}{ds} \simeq \frac{\lambda'(N)-\lambda(N)}{\epsilon'} \quad \text{and} \quad \frac{d^2\lambda}{dN\,ds} \simeq \frac{\dfrac{d\lambda'}{dN}-\dfrac{d\lambda}{dN}}{\epsilon'}$$

7. Solve the following 2×2 system for ΔN, Δs

$$\begin{bmatrix} \dfrac{d\lambda}{ds} & \dfrac{d\lambda}{dN} \\ \dfrac{d^2\lambda}{dNds} & \dfrac{d^2\lambda}{dN} \end{bmatrix} \begin{bmatrix} \Delta s \\ \Delta N \end{bmatrix} = \begin{bmatrix} -\lambda \\ -\dfrac{d\lambda}{dN} \end{bmatrix}$$

and set $y^{k+1} = z^k + \Delta s\, v^k$, $N^{k+1} = N^k + \Delta N$

8. While ΔN or $\Delta s > \epsilon''$ Go To (1)

Given a good initial guess, this algorithm ultimately converges quadratically even if the path of onset of ribbing points lies close to a fold surface. However, it is rather inefficient, as it requires 8 LU decompositions per iteration. By contrast, an algorithm similar to Poenisch and Schwetlick's (1981) would require only 2 LU decompositions (one of J and another of J_{3D}) and a few back-solves per iteration, but is more difficult to implement and is not employed in this work. Typical values for the perturbations to achieve quadratic convergence on the CRAY C-90 are $\epsilon = 10^{-2}$, $\epsilon' = 10^{-3}$; the tolerance ϵ'' was set to 10^{-6}.

Manuscript received Mar. 25, 1997, and revision received July 18, 1997.